Tomographic completeness and robustness of quantum reservoir networks

Tanjung Krisnanda,[1,2,*] Huawen Xu,[1] Sanjib Ghosh,[3,†] and Timothy C. H. Liew[1,4]

[1]*School of Physical and Mathematical Sciences, Nanyang Technological University, 637371 Singapore, Singapore*
[2]*Centre for Quantum Technologies, National University of Singapore, 3 Science Drive 2, 117543 Singapore, Singapore*
[3]*Beijing Academy of Quantum Information Sciences, West Building 3, No. 10 Xibeiwang East Road, Haidian District, Beijing 100193, China*
[4]*MajuLab, International Joint Research Unit UMI 3654, CNRS, Université Côte d'Azur, Sorbonne Université, National University of Singapore, Nanyang Technological University, Singapore*

(Received 19 July 2022; revised 9 December 2022; accepted 22 March 2023; published 4 April 2023)

Quantum reservoir processing offers an option to perform quantum tomography of input objects by postprocessing quantities, obtained from local measurements, from a quantum reservoir network that has interacted with the former. We develop a method to assess a tomographic completeness criterion for arbitrary quantum reservoir architectures. Furthermore, we propose a figure of merit that quantifies their robustness against imperfections. Measured quantities from the reservoir nodes correspond to effective observables acting on the input objects, and we provide a way to retrieve them. Finally, we present examples of quantum tomography for demonstration. Our general method offers guidance in optimizing implementations of quantum reservoir processing.

DOI: 10.1103/PhysRevA.107.042402

I. INTRODUCTION

Quantum neural networks (QNNs) have surfaced as a form of artificial neural network constructed with quantum systems [1]. The goal is normally to carry out either classical tasks with superiority compared to classical neural networks (CNNs), or quantum tasks that are impossible with CNNs. For example, see the recent works that proposed QNNs with different architectures and machine learning techniques [2–6]. Granted that extreme controls over quantum systems are expensive resources, an alternative that relaxes this condition is worth exploring. Inspired by a CNN architecture known as reservoir computing [7,8], where one does not require controls over the network itself, quantum versions have been recently proposed for solving both classical tasks [4], such as time series prediction [9] or pattern prediction [10], and quantum tasks [5], such as quantum state tomography [11–13], quantum process tomography [14], quantum state preparation [15,16], quantum operations [17], and quantum metrology [18] (see Ref. [19] for a review).

In the area of classical tasks, quantum reservoir computers are understood to benefit from nonlinearity [20,21], the large size of the quantum Hilbert space [22–24], and they show enhanced performance at phase transition boundaries [25,26]. Their physical realization has been considered using nuclear spins [27] or Rydberg atoms [28], and the general proofs of their universality have been established [29–32]. However, the mechanism by which quantum reservoirs process quantum information in quantum tasks is less well understood, and there are no obvious figures of merit of a given quantum reservoir, at least before looking at the results from a testing set of data.

Here we will focus on the use of quantum reservoir processing (QRP) to perform quantum state tomography. In this task, an input quantum state interacts with quantum systems forming the quantum reservoir network (QRN), which undergo dynamical evolution before the state of network nodes is measured (possibly at specific times). The objective is to reconstruct the input quantum state via linear combinations of the measured quantities, which can be seen as the application of a trained output processing layer within the QRP architecture. By identifying the action of the QRN as a linear map acting on the input quantum state, we find that the output layer of the QRP essentially inverts this map. However, while the linear map corresponding to the action of the QRN maps a quantum state to readily observable quantities, the inverse map maps these quantities to a representation of the input quantum state (e.g., elements of its density matrix). In practice, the inverse map is learned through training with known input-output examples in a procedure known as ridge regression. We show that this procedure is indeed equivalent to forming the inverse map.

Having established clearly the formal mechanism of QRP for quantum tomography, we present a way to assess whether a QRP is tomographically complete (i.e., able to estimate the state of an input object *completely*) based on the map. Furthermore, we access its robustness in the presence of a range of imperfections, including quantum noises, fluctuation of system parameters, and measurement errors. We identify the condition number of the QRN map as a key figure of merit that quantifies its robustness in the presence of the considered imperfections. Note that this figure of merit is also a property of the QRN itself and is independent of the training procedure or any testing data. Consequently, this introduces a quantitative way of comparing different QRN architectures without benchmarking different input states at the testing level.

To complete the picture, we show how to relate the measured quantities obtained from the QRN nodes to effective

*tanjung@nus.edu.sg
†sanjibghosh@baqis.ac.cn

 ©2023 American Physical Society

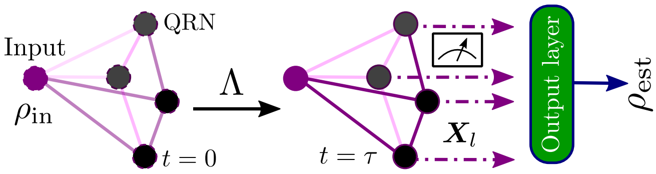

FIG. 1. An input object with dimension d, whose state is $\rho_{\rm in}$, interacts with quantum reservoir nodes for a time τ. The general dynamics is represented by a completely positive and trace-preserving map Λ. At time τ, simple quantities are measured from the reservoir nodes $\{X_l\}_{l=1}^{L}$, which will be postprocessed via a trained output layer. The final output is an estimate of the input state $\rho_{\rm est}$.

observables acting on the input quantum states. For demonstration, we test our method for simple cases, where we model one- and two-qubit tomography. We note that the method developed in this paper is general, and it may be used for general QNNs aimed at recognizing properties of input quantum states.

II. THE GENERAL FRAMEWORK

Quantum tomography with QRP (see Fig. 1) generally incorporates (i) to-be-measured input objects, (ii) a QRN whose nodes are made of interacting quantum systems, and (iii) an output layer that includes postprocessing the measured quantities from the QRN nodes. The signature of this platform is that it is versatile and experimentally friendly. In particular, it can allow processing input objects of any dimension, having random or less-controlled quantum systems as the QRN, and simpler measurements (only local) conducted on the QRN nodes. The last part could provide a better alternative compared to direct measurements, especially those requiring conditional or correlation measurements. The scheme is also particularly useful for cases in which the to-be-measured objects are not accessible for direct measurements.

To write the general formalism of the scheme described above, let us start with the input objects. An object with dimension d has $d^2 - 1$ independent parameters, which one can use to reconstruct its state $\rho_{\rm in}$. We shall refer to an ideal tomography, where all the parameters $\{Y_m\}_{m=1}^{d^2-1}$ (or simply Y, written in a vector form) can be estimated with QRP, as satisfying the *tomographic completeness* criterion. The analysis presented in this paper holds for any parametrization of the input state.

The dynamics of the whole system evolves the initial state $\rho(0) = \rho_{\rm in} \otimes \rho_{\rm QRN}(0)$ to $\rho(\tau)$ for a time τ. In general, we take the evolution as a completely positive and trace-preserving (CPTP) map acting on the initial state, i.e., $\rho(\tau) = \Lambda[\rho(0)]$. This includes dynamics such as that described within the Lindblad master equation normally assumed for QRP proposals [19].

After obtaining the state of the QRN at τ, $\rho_{\rm QRN}(\tau) = {\rm tr}_{\rm in}(\rho(\tau))$, where ${\rm tr}_{\rm in}$ denotes the partial trace with respect to the input object, one then performs the simpler local measurements on the QRN nodes. Let us write the measured observables in a vector form X, where the lth element reads $X_l = {\rm tr}(\rho(\tau)\mathbb{1}_d \otimes \hat{X}_l) = {\rm tr}_{\rm QRN}(\rho_{\rm QRN}(\tau)\hat{X}_l)$, with $l = 1, 2, \ldots, L$, and $\hat{X}_l$ is an operator acting on a QRN node. The role of the output layer is to combine the measured observables linearly to estimate $d^2 - 1$ parameters of $\rho_{\rm in}$. In particular,

$$Y_{\rm est} = \mathcal{W}X + C, \tag{1}$$

where the weight matrix $\mathcal{W}$ and bias vector C are obtained via training. This completes the tomography, where one ends up with an estimated state $\rho_{\rm est}(Y_{\rm est})$. The training can be performed with known sets of input-output $\{Y, X\}$ with ridge regression [19], see Appendix A for more detail.

Having described the general framework, we emphasize that not all quantum reservoir architectures satisfy the tomographic completeness criterion, i.e., Eq. (1) *does not* always work as Y may not equal $\mathcal{W}X + C$. Below we provide a universal way to assess this criterion.

III. TOMOGRAPHIC COMPLETENESS CRITERION

It is apparent that each observable X_l is a linear function of the elements of $\rho_{\rm QRN}(\tau)$, whose elements are obtained linearly from those of $\rho(\tau)$. The latter is also obtained linearly from $\rho(0)$ as the dynamics is an action of a CPTP map. This means that X and Y can be written as

$$X = \mathcal{M}Y + V, \tag{2}$$

where $\mathcal{M}$ is an effective map and V is a constant vector.

For a given choice of parametrization, a QRN architecture (that governs the dynamics), and measured QRN observables, Eq. (2) *always holds* and it is quite straightforward to compute the effective map $\mathcal{M}$ and vector V numerically. It is the center for the analyses presented in this paper, from which one can assess the tomographic completeness criterion and robustness of the scheme.

A QRP satisfies the tomographic completeness criterion if the following requirement holds:

$$\det(\mathcal{M}^\dagger\mathcal{M}) \neq 0. \tag{3}$$

The statement above is justified as follows. First, from Eqs. (1) and (2), we write $Y_{\rm est} = \mathcal{W}(\mathcal{M}Y + V) + C$. We stress here that $\mathcal{M}$ and V are fixed and given by a particular QRN architecture, while $\mathcal{W}$ and C are optimized via training. An ideal outcome, i.e., perfect state reconstruction $Y_{\rm est} = Y$, is given if $\mathcal{W} = \mathcal{M}^+$ and $C = -\mathcal{M}^+V$. Here, $\mathcal{M}^+ = (\mathcal{M}^\dagger\mathcal{M})^{-1}\mathcal{M}^\dagger$ is a left Moore-Penrose pseudoinverse of the map $\mathcal{M}$ such that $\mathcal{M}^+\mathcal{M} = \mathbb{1}$. This necessitates the existence of the left pseudoinverse, which is essentially the invertibility of $\mathcal{M}^\dagger\mathcal{M}$, and therefore, Eq. (3). We note an immediate consequence of Eq. (3) is that $L \geqslant d^2 - 1$. This follows as $\det(\mathcal{M}^\dagger\mathcal{M}) = 0$ for any rectangular map $\mathcal{M}$ having fewer rows than columns ($L < d^2 - 1$). For the minimum case of $L = d^2 - 1$, we have a square map $\mathcal{M}$, and the condition for an ideal outcome reduces to $\det(\mathcal{M}) \neq 0$.

In real situations, where the QRN is not controlled, the dynamics is treated as a *black box*. In this case, one guesses Eq. (1), where the weights and biases of the output layer ($\mathcal{W}$ and C) are obtained from training; see Appendix A. It is important to note that similar training can also be performed to obtain $\mathcal{M}$ and V of Eq. (2), which is guaranteed to hold. This allows one to assess the tomographic completeness criterion and the figure of merit for robustness, as we shall show below, without the need for testing data.

IV. ROBUSTNESS

Once a QRP satisfies the tomographic completeness criterion, we can now discuss its robustness. In experiments, imperfections may come from quantum noises such as energy decay, dephasing, and depolarizing noise; fluctuations of the system parameters such as coupling strengths, pumping strengths, etc.; and measurement errors from finite measurement instances. Quantum noises cause loss of information regarding the input objects. The fluctuation in dynamical parameters translates to a fluctuating effective map $\mathcal{M}$, which causes inconsistencies in the input-output relation; see Eq. (2). Furthermore, finite measurements cause errors on the measured QRN observables, which contribute to inaccuracies in the estimated state $\rho_{\text{est}}(\boldsymbol{X})$; see Eq. (1).

We can use the condition number of the effective map as a *figure of merit* that quantifies the robustness of a QRP against general imperfections, i.e.,

$$\eta \equiv ||\mathcal{M}||\,||\mathcal{M}^{+}||, \tag{4}$$

where $||\cdot||$ denotes the Euclidean norm. For a linear equation, such as Eq. (2), the condition number characterizes the accuracy of the solution $\boldsymbol{Y}$ with respect to perturbations (errors) in the map δM or observables δX with $\delta \ll 1$; see Refs. [33,34]. In particular, if η is small (close to unity), the map $\mathcal{M}$ is well conditioned and the perturbations will translate to small errors in the solution. On the other hand, high η leads to perturbations causing high errors in the solution. In our case, δX incorporates measurement errors, while δM incorporates those coming from fluctuations of the system parameters. We note that bounds exist on the relative error in the solution in terms of that of the map or the observables, where the condition number is shown as an important factor [34].

Furthermore, Eq. (4) can be written as $\eta = \Xi_{\max}(\mathcal{M})/\Xi_{\min}(\mathcal{M})$, where $\Xi_{\max(\min)}(\cdot)$ denotes the maximum (minimum) singular value of a matrix. The loss of information induced by quantum noises is reflected in the weaker dependence of $\boldsymbol{X}$ with respect to $\boldsymbol{Y}$; see Eq. (2). This results in smaller elements of the effective map $\mathcal{M}$, which in turn causes $\Xi_{\min}(\mathcal{M})$ to decrease (more dominant), and therefore it increases η. This completes the justification for the figure of merit in Eq. (4). We also note that the determinant of the map can be used as a figure of merit; see Appendix B for details.

V. EFFECTIVE MEASUREMENT PICTURE

From a quantum information perspective, as one expects, the tomographic process with QRP can be interpreted as effective measurements directly targeted at the input objects. To illustrate this point, let us start with

$$\boldsymbol{X}_l = \text{tr}(\rho(\tau)\mathbb{1}_d \otimes \hat{X}_l) = \text{tr}_{\text{in}}(\rho_{\text{in}}\hat{Z}_{\text{eff},l}), \tag{5}$$

where $\hat{Z}_{\text{eff},l}$ is the corresponding effective observable acting on the input objects, and the steps are justified as follows. By explicitly writing the dynamics and initial state, we have $\text{tr}(\rho(\tau)\mathbb{1}_d \otimes \hat{X}_l) = \text{tr}(\Lambda[\rho_{\text{in}} \otimes \rho_{\text{QRN}}(0)]\mathbb{1}_d \otimes \hat{X}_l) = \text{tr}(\rho_{\text{in}} \otimes \rho_{\text{QRN}}(0)\tilde{\Lambda}[\mathbb{1}_d \otimes \hat{X}_l])$, where in the second equality we switch from a Schrödinger to a Heisenberg picture, with the evolution performed on the observable instead with a map $\tilde{\Lambda}$. Next, we carry out the partial trace with respect to the QRN nodes to (in principle) arrive at Eq. (5).

Alternatively, one can numerically retrieve the effective observable $\hat{Z}_{\text{eff},l}$ that is a result of QRN observable $\hat{X}_l$ from the effective map $\mathcal{M}$ and constant vector $\boldsymbol{V}$, with the help of Eq. (2), as follows. First, note that all complete parameters of the input state are basically measured observables that one can obtain through *tomographically complete* measurements, should direct measurements on the input objects be possible. These parameters can be written as $\{\boldsymbol{Y}_m\}_{m=1}^{d^2-1} = \{\text{tr}_{\text{in}}(\rho_{\text{in}}\hat{Y}_m)\}_{m=1}^{d^2-1}$, where $\hat{Y}_m$ is the corresponding measurement observable for $\boldsymbol{Y}_m$. From Eq. (2), the lth QRN observable reads

$$\begin{aligned}\boldsymbol{X}_l &= \sum_m \mathcal{M}_{l,m}\boldsymbol{Y}_m + \boldsymbol{V}_l \\ &= \text{tr}_{\text{in}}\left(\rho_{\text{in}}\left(\sum_m \mathcal{M}_{l,m}\hat{Y}_m + \mathbb{1}_d\boldsymbol{V}_l\right)\right),\end{aligned} \tag{6}$$

where we have used $\boldsymbol{Y}_m = \text{tr}_{\text{in}}(\rho_{\text{in}}\hat{Y}_m)$. Therefore, the effective observable can be written as $\hat{Z}_{\text{eff},l} = \sum_m \mathcal{M}_{l,m}\hat{Y}_m + \mathbb{1}_d\boldsymbol{V}_l$. It is clear that having *at least* d^2-1 independent rows of $\mathcal{M}$ is essential for the QRP scheme as it allows the effective observables to be tomographically complete for estimating ρ_{in}. We note that this is equivalent to the requirement in Eq. (3).

VI. EXEMPLARY QUANTUM TOMOGRAPHY

Now, we provide demonstrations with simple models to gain insight of QRP. First, suppose we have two interacting qubits, where one is assigned as the input and the other as the QRN; see Fig. 2(a). Let us take the Hamiltonian as

$$\hat{H}/\hbar = w_1\hat{\sigma}_1^z + w_2\hat{\sigma}_2^z + K_{12}(\hat{\sigma}_1^+\hat{\sigma}_2^- + \hat{\sigma}_2^+\hat{\sigma}_1^-) + P_2\hat{\sigma}_2^x, \tag{7}$$

where the subscripts indicate the subsystem, $\hat{\sigma}^{+(-)}$ is the raising (lowering) operator, K_{12} is the hopping type interaction, $w_{1,2}$ is the frequency, and P_2 is the coherent pump. We have used $\hat{\sigma}^{x,y,z}$ to denote the Pauli matrices.

Let us also consider a decay mechanism affecting the second qubit to illustrate a loss of information. In particular, the dynamics follows the Lindblad master equation $\dot{\rho} = -i[\hat{H},\rho]/\hbar + (\gamma_2/2)\mathcal{L}(\rho,\hat{\sigma}_2^-)$, where $\mathcal{L}(\rho,\hat{\sigma}_2^-) = 2\hat{\sigma}_2^-\rho\hat{\sigma}_2^+ - \{\hat{\sigma}_2^+\hat{\sigma}_2^-,\rho\}$, γ_2 denotes the strength of the decay, and the state is initialized as $\rho(0) = \rho_{\text{in}} \otimes |0\rangle\langle 0|$. For simulations, as one QRN realization, we take random dynamical parameters $\{w_1, w_2, K_{12}, P_2, 5\gamma_2\} \in [1,2] \times \Omega$, where Ω is the overall strength in units of frequency.

For the parametrization, let us take $\{\boldsymbol{Y}_m\}_{m=1}^3 = \{\rho_{\text{in}}(1,1), \text{Re}(\rho_{\text{in}}(1,2)), \text{Im}(\rho_{\text{in}}(1,2))\}$ from which one can reconstruct ρ_{in} completely. To demonstrate one of the advantages of the scheme, we will utilize time-multiplexing. In particular, we take $\{\boldsymbol{X}_l\}_{l=1}^3 = \{\text{tr}(\rho(\tau_1)\hat{\sigma}_2^z), \text{tr}(\rho(\tau_2)\hat{\sigma}_2^z), \text{tr}(\rho(\tau_3)\hat{\sigma}_2^z)\}$. One can now follow our method and retrieve the effective map $\mathcal{M}$.

Next, we test the performance of the scheme by generating random input states $\{\rho_{\text{in},n}\}_{n=1}^{N_{\text{test}}}$; see Appendix C for details. Each of the input states is evolved, after which one obtains the corresponding measured QRN observables $\{\boldsymbol{X}_l\}_{l=1}^3$. To incorporate errors coming from finite measurement instances,

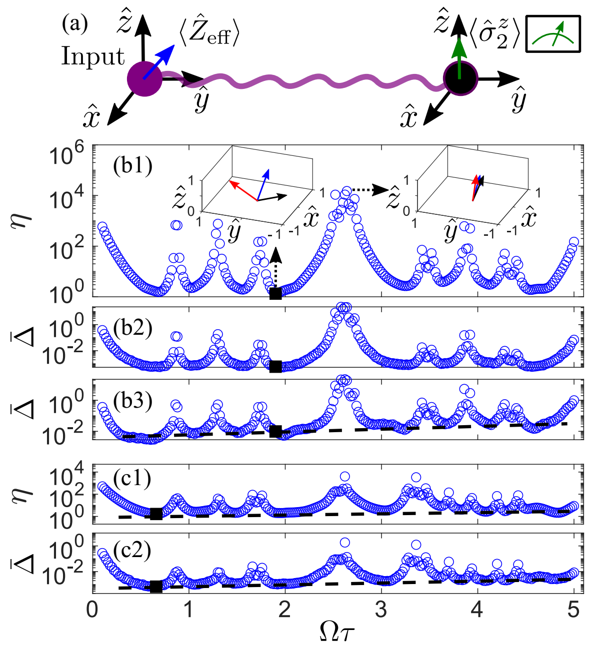

FIG. 2. (a) Illustration of the setup, where a QRN observable is seen as an effective measurement on the input. Panels (b1)–(c2) represent results from an exemplary realization of QRN parameters. (b1) The figure of merit $\eta = ||\mathcal{M}||\,||\mathcal{M}^{+}||$ without decay. The insets show the direction of the effective observables. (b2) The corresponding tomographic errors, taking into account measurement errors. (b3) Similar to (b2) with the addition of fluctuations of the dynamical parameters. (c1) The figure of merit with decay. (c2) The corresponding tomographic errors. Dashed lines represent overall trend. Black dots denote minimum η and the corresponding error $\bar{\Delta}$.

we update each observable as $\boldsymbol{X}_l \to \boldsymbol{X}_l + \varepsilon_l$, where ε_l is sampled from a normal distribution with zero mean and standard deviation ξ. Note that from the central limit theorem, we have $\xi \propto 1/\sqrt{S}$, where S is the number of measurement instances. In what follows, we take $\xi = 10^{-3}$. Knowing $\{\boldsymbol{X}_l\}_{l=1}^{3}$, one estimates the input state by utilizing Eq. (1). As a quantity to represent tomographic estimation error, we use $\Delta = \sum_m |\boldsymbol{Y}_m - \boldsymbol{Y}_{\text{est},m}|/(d^2-1)$. Furthermore, for one QRN realization we test $N_{\text{test}} = 100$ randomly generated input states, for which the average error is denoted as $\bar{\Delta}$.

The simulation results are presented in Figs. 2(b1)–2(c2) for an exemplary realization of QRN parameters. For ease of demonstration, we have taken a constant time interval, i.e., $\tau_n = n\tau$. First, panel (b1) shows the figure of merit η without decay, i.e., $\gamma_2 = 0$. Note that as we have $L = d^2 - 1 = 3$ and that $\det(\mathcal{M}) \neq 0$ for most of τ (shown in the SM), this QRN architecture satisfies the tomographic completeness criterion most of the time. Furthermore, we have indicated with a black dot the minimum η, for which the QRP is most robust. For performance test, we plotted the tomographic errors in panel (b2), where we have incorporated measurement errors. One can see that $\bar{\Delta}$ follows the trend of the figure of merit η, confirming the quality of the latter.

Next, we incorporated imperfections coming from fluctuations of the dynamical parameters. We evolved each of the initial states during testing by adding random strengths $\nu \in [-1, 1] \times 10^{-2} \times \Omega$ to the QRN parameters. The tomographic errors are plotted in panel (b3), showing similar behavior to panel (b2) except for an overall increasing trend (dashed line). As the dynamics runs for longer time, the fluctuations on the dynamical parameters result in stronger error of the effective map, and at some point the assumption $\delta \ll 1$ for the effective map $\mathcal{M} + \delta M$ is no longer valid. In this case, η still provides a good figure of merit for $3|\nu|\tau \ll 1$.

We now include the energy decay γ_2 in the dynamics, which directly affects the effective map, and hence η; see panel (c1). The loss of information in the system causes weaker elements of $\mathcal{M}$, resulting in the increasing overall trend (dashed line). The corresponding tomographic errors during testing are plotted in panel (c2). One can see that the error $\bar{\Delta}$ is anticipated by the figure of merit η, including the overall increasing trend (dashed line).

After computing the effective map, we also computed the corresponding effective measurement operators $\{\hat{Z}_{\text{eff},1}, \hat{Z}_{\text{eff},2}, \hat{Z}_{\text{eff},3}\}$. Note that the elements of ρ_{in} are related to measurements of Pauli matrices, i.e., $\boldsymbol{Y}_1 = \text{tr}(\rho_{\text{in}}(\hat{\sigma}_1^z + \mathbb{1}_2)/2)$, $\boldsymbol{Y}_2 = \text{tr}(\rho_{\text{in}}(\hat{\sigma}_1^x/2))$, and $\boldsymbol{Y}_3 = \text{tr}(\rho_{\text{in}}(-\hat{\sigma}_1^y/2))$. Consequently, the rows of $\mathcal{M}$ are vectors representing measurements, seen from the Bloch sphere. For example, see the insets of Fig. 2(b1), showing the vectors when η is low (left) and high (right). The relative angles between these vectors, for which η is minimum for the scenario described in panel (b1) with time interval $\tau \in [0, 3]/\Omega$, are $\Theta_{12} = 87^\circ \pm 19^\circ$, $\Theta_{23} = 82^\circ \pm 10^\circ$, and $\Theta_{13} = 90^\circ \pm 19^\circ$, where we performed the test over 50 different QRN realizations. In the ideal case, it is expected that the angles are 90°, corresponding to *orthogonal measurements*.

We also performed simulations for two-qubit tomography; see Appendix D for details.

VII. DISCUSSION

It is important to note that for any QRP satisfying the tomographic completeness criterion, the tomographic error $\Delta \to 0$ in the limit of no measurement errors and fluctuations of dynamical parameters, i.e., $\xi \to 0$ and $\nu \to 0$. This is because the effective map $\mathcal{M}^{+}$ exists such that the input parameters can be obtained *exactly* given the measured QRN observables, as written in Eq. (1). This is still true in the presence of quantum noises such as energy decay, dephasing, and depolarization affecting the involved quantum systems as long as their strengths are constant.

The experimentally friendly platform of quantum reservoir processing makes it attractive for physical implementations. Possibilities for qubits as the QRN nodes include Rydberg atoms [35,36], fermionized photons [37], optically trapped atoms [38], and superconducting qubits [39,40]. We also note that the QRN can be constructed from bosonic modes, e.g., with coupled cavities [41]. We anticipate that the method developed in this paper can be used in all the cases above and that it would help to design architectures satisfying the tomographic completeness criterion and optimize robustness against imperfections.

VIII. CONCLUSION

We have shown the origin of quantum reservoir processing for quantum state tomography. We developed a method to test whether a quantum reservoir architecture satisfies the tomographic completeness criterion, where the system can estimate arbitrary states of input objects completely. Furthermore, we proposed a figure of merit that quantifies the robustness of a given architecture against general imperfections, e.g., quantum noises, fluctuations of the dynamical parameters, and measurement errors. This allows a quantitative comparison of different architectures, without the need for benchmarking different input states at the testing level. We interpreted the action of performing measurements on the QRN nodes as effective measurements on the input objects, and we provided a way to retrieve the latter. Finally, we demonstrated our methods for simple cases of one- and two-qubit tomography.

ACKNOWLEDGMENTS

T.K. thanks Yvonne Gao for hospitality at National University of Singapore. T.K., H.X., and T.C.H.L. were supported by the Singapore Ministry of Education under its AcRF Tier 2 Grant No. T2EP50121-0006. S.G. acknowledges funding support from the Excellent Young Scientists Fund Program (Overseas) of China, and the National Natural Science Foundation of China (Grant No. 12274034).

APPENDIX A: TRAINING WITH RIDGE REGRESSION

Here we present details to obtain the weights $\mathcal{W}$ and biases $\boldsymbol{C}$ of the output layer. First, let us assume that the QRP we consider satisfies the tomographic completeness criterion. We start with Eq. (2) in the main text, which always holds, and we use $-\mathcal{M}^{+}\boldsymbol{V} = \boldsymbol{C}$. Then, we can write $\boldsymbol{Y} = \mathcal{M}^{+}\boldsymbol{X} + \boldsymbol{C}$ or equivalently

$$[\boldsymbol{C} \quad \mathcal{M}^{+}]\begin{bmatrix} 1 \\ \boldsymbol{X} \end{bmatrix} = \boldsymbol{Y}. \tag{A1}$$

The goal is essentially to find the left matrix, which contains the weights and biases of the output layer, i.e., $[\boldsymbol{C} \;\; \mathcal{W}]$.

This is done with ridge regression by using known sets of input and output $\{\boldsymbol{Y}_{(n)}, \boldsymbol{X}_{(n)}\}_{n=1}^{N_{\rm tr}}$, where we have used (n) as the label, and $N_{\rm tr}$ denotes the number of sets. We define a matrix of inputs $\mathcal{Y}$ and outputs $\mathcal{X}$ as

$$\mathcal{Y} = [\boldsymbol{Y}_{(1)} \quad \boldsymbol{Y}_{(2)} \quad \cdots \quad \boldsymbol{Y}_{(N_{\rm tr})}],$$
$$\mathcal{X} = \begin{bmatrix} 1 & 1 & \cdots & 1 \\ \boldsymbol{X}_{(1)} & \boldsymbol{X}_{(2)} & \cdots & \boldsymbol{X}_{(N_{\rm tr})} \end{bmatrix}. \tag{A2}$$

The ridge regression formula then reads

$$[\boldsymbol{C} \;\; \mathcal{W}] = \mathcal{Y}\mathcal{X}^{T}(\mathcal{X}\mathcal{X}^{T} + \phi\mathbb{1})^{-1}, \tag{A3}$$

where ϕ is the regularization coefficient.

We note that for the performance test in Fig. 2 in the main text, the weight and biases of the output layer are directly computed from the effective map $\mathcal{M}$ and constant vector $\boldsymbol{V}$, i.e., $\mathcal{W} = \mathcal{M}^{+}$ and $\boldsymbol{C} = -\mathcal{M}^{+}\boldsymbol{V}$. Next, this output layer is used in testing, from which we present the tomographic estimation errors. In practice, the weight and biases of the output layer are obtained from training data, as explained in this section. To demonstrate this, let us consider the setup of Fig. 2(b2) in the main text with time-multiplexing constant $\tau = 1.9/\Omega$. We generated $N_{\rm tr} = 10$ training data, i.e., the input and corresponding output $\{\boldsymbol{Y}_{(n)}, \boldsymbol{X}_{(n)}\}_{n=1}^{10}$, where we have used a larger measurement error strength $\xi = 10^{-2}$ for better demonstration. Training with ridge regression is performed to obtain the weight and biases of the output layer; see Eq. (A3) above. For different regularization coefficients, we computed the corresponding tomographic estimation errors from the training data; see Fig. 3 showing a typical trend. In particular, small ϕ results in overfitting, whereas large ϕ leads to underfitting. The minimum error is referred to as a sweet spot, which gives the chosen ϕ in practice.

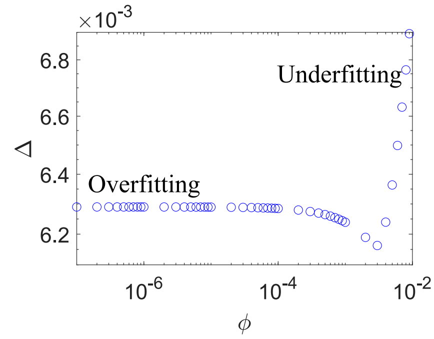

FIG. 3. Tomographic estimation errors from the training data for the setup of Fig. 2(b2) in the main text ($\tau = 1.9/\Omega$) against regularization coefficient ϕ.

APPENDIX B: DETERMINANT OF THE MAP

Here, we provide an alternative figure of merit representing the robustness of QRP against general imperfections. Recall the requirement of having $L \geqslant d^2 - 1$ in the main text. First, let us assume a square map $\mathcal{M}$, which is the case when $L = d^2 - 1$. In this case, the tomographic completeness criterion is $\det(\mathcal{M}) \neq 0$. For the strict case of $L > d^2 - 1$, one can still form a square map $\mathcal{M}$ by choosing $d^2 - 1$ of the L observables (the order does not matter), and form the linear equation as in Eq. (2) in the main text. There are $L!/(d^2-1)!(L-d^2+1)!$ possibilities from which one can choose, and to satisfy the tomographic completeness criterion, at least one choice should give $\det(\mathcal{M}) \neq 0$.

Now, recall that the absolute value of the determinant of a linear map represents the ratio of the volume of the changes in $\boldsymbol{X}$ and $\boldsymbol{Y}_{\rm est}$, i.e., $\partial \boldsymbol{X}_1 \cdots \partial \boldsymbol{X}_{d^2-1} = |\det(\mathcal{M})|\, \partial \boldsymbol{Y}_{{\rm est},1} \cdots \partial \boldsymbol{Y}_{{\rm est},d^2-1}$. First, it is immediately apparent that errors in $\boldsymbol{X}$ (finite measurements) will result in small errors when estimating $\boldsymbol{Y}_{\rm est}$ for higher values of $|\det(\mathcal{M})|$. Second, the loss of information caused by quantum noises is reflected in the weaker dependence of $\boldsymbol{X}$ with respect to $\boldsymbol{Y}$; see Eq. (2) in the main text. In other words, we will have smaller coefficients or elements of the effective map $\mathcal{M}$, making $|\det(\mathcal{M})|$ smaller. Last but not least, suppose we have a map $\mathcal{M} + \delta M$, where the last term is a result of fluctuations of the system parameters and $\delta \ll 1$. The solution for Eq. (1) now reads $\boldsymbol{Y}'_{\rm est} \approx \mathcal{M}^{-1}(\mathbb{1} - \delta M \mathcal{M}^{-1})(\boldsymbol{X} - \boldsymbol{V})$, where we have used a first-order approximation for $(\mathcal{M} + \delta M)^{-1}$, and $\boldsymbol{Y}'_{\rm est}$ denotes the new estimated vector. By simplifying further, we have $\boldsymbol{Y}'_{\rm est} - \boldsymbol{Y}_{\rm est} \approx \mathcal{M}^{-1}(-\delta M \boldsymbol{Y}_{\rm est})$. Consequently, a small change in the estimated vector as a result of the fluctuation term is given when $|\det(\mathcal{M})|$ is high. Therefore,

$$\zeta \equiv |\det(\mathcal{M})| \tag{B1}$$

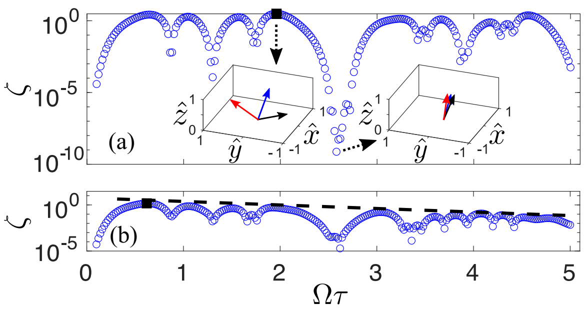

FIG. 4. Determinant of the map as a figure of merit for one-qubit tomography. (a) ζ for the case of Fig. 2(b1) in the main text. (b) ζ for the case of Fig. 2(c1) in the main text.

quantifies the robustness of QRP against general imperfections. We note that ζ quantifies robustness in the opposite way to that of η. In particular, higher values of ζ would imply a more robust QRP architecture.

For one-qubit tomography, we present the quantity ζ in Figs. 4(a) and 4(b), respectively, for the case of Figs. 2(b1) and 2(c1) in the main text. For two-qubit tomography, we present ζ in Figs. 5(a) and 5(b), respectively, for the case of Figs. 6(a1) and 6(b1). One can see that the tomographic errors behave opposite to the corresponding ζ. It can also be seen that ζ accounts for the overall increasing or decreasing trend of the tomographic errors with respect to $\Omega\tau$ (dashed lines).

APPENDIX C: RANDOM INPUT STATES

The random input states used at the testing level are generated as follows. First, we generate a $d \times d$ matrix G, where d is the dimension of the input object. Each element of G is taken as

$$G_{ij} = 2(\alpha + i\beta) - (1 + i), \tag{C1}$$

where α and β are sampled from a normal distribution with zero mean and standard deviation of 1. Next, a Hermitian matrix is generated as

$$H = G + G^\dagger, \tag{C2}$$

which one can use to generate an input state,

$$\rho_{\text{in}} = \frac{H^2}{\text{tr}(H^2)}. \tag{C3}$$

APPENDIX D: TWO-QUBIT TOMOGRAPHY

Here we show that it is possible to perform tomography on two-qubit input states by using a single-qubit QRN. The setup takes the following Hamiltonian:

$$\begin{aligned}\hat{H}/\hbar = {} & w_1\hat{\sigma}_1^z + w_2\hat{\sigma}_2^z + w_3\hat{\sigma}_3^z + K_{13}(\hat{\sigma}_1^+\hat{\sigma}_3^- + \hat{\sigma}_3^+\hat{\sigma}_1^-) \\ & + K_{23}(\hat{\sigma}_2^+\hat{\sigma}_3^- + \hat{\sigma}_3^+\hat{\sigma}_2^-) + P_3\hat{\sigma}_3^x,\end{aligned} \tag{D1}$$

where the subscripts $\{1, 2\}$ indicate the input qubits, while 3 indicates the QRN qubit. To demonstrate loss of information, suppose that the QRN qubit undergoes energy decay with a rate γ_3. The dynamics follows,

$$\dot{\rho} = -\frac{i}{\hbar}[\hat{H}, \rho] + \frac{\gamma_3}{2}\mathcal{L}(\rho, \hat{\sigma}_3^-), \tag{D2}$$

with the initial state taken as $\rho(0) = \rho_{\text{in}} \otimes |0\rangle\langle 0|$. Similar to the one-qubit tomography in the main text, we randomize the parameters as $\{w_1, w_2, w_3, K_{13}, K_{23}, P_3, 5\gamma_3\} \in [1, 2] \times \Omega$.

Furthermore, as the parametrization for the input state and measured QRN observables we use

$$\boldsymbol{Y} = \begin{bmatrix} \rho_{\text{in}}(1,1) \\ \rho_{\text{in}}(2,2) \\ \rho_{\text{in}}(3,3) \\ \text{Re}(\rho_{\text{in}}(1,2)) \\ \text{Im}(\rho_{\text{in}}(1,2)) \\ \text{Re}(\rho_{\text{in}}(1,3)) \\ \text{Im}(\rho_{\text{in}}(1,3)) \\ \text{Re}(\rho_{\text{in}}(1,4)) \\ \text{Im}(\rho_{\text{in}}(1,4)) \\ \text{Re}(\rho_{\text{in}}(2,3)) \\ \text{Im}(\rho_{\text{in}}(2,3)) \\ \text{Re}(\rho_{\text{in}}(2,4)) \\ \text{Im}(\rho_{\text{in}}(2,4)) \\ \text{Re}(\rho_{\text{in}}(3,4)) \\ \text{Im}(\rho_{\text{in}}(3,4)) \end{bmatrix}, \quad \boldsymbol{X} = \begin{bmatrix} \text{tr}(\rho(\tau)\hat{\sigma}_3^z) \\ \text{tr}(\rho(2\tau)\hat{\sigma}_3^z) \\ \text{tr}(\rho(3\tau)\hat{\sigma}_3^z) \\ \text{tr}(\rho(4\tau)\hat{\sigma}_3^z) \\ \text{tr}(\rho(5\tau)\hat{\sigma}_3^z) \\ \text{tr}(\rho(6\tau)\hat{\sigma}_3^z) \\ \text{tr}(\rho(7\tau)\hat{\sigma}_3^z) \\ \text{tr}(\rho(8\tau)\hat{\sigma}_3^z) \\ \text{tr}(\rho(9\tau)\hat{\sigma}_3^z) \\ \text{tr}(\rho(10\tau)\hat{\sigma}_3^z) \\ \text{tr}(\rho(11\tau)\hat{\sigma}_3^z) \\ \text{tr}(\rho(12\tau)\hat{\sigma}_3^z) \\ \text{tr}(\rho(13\tau)\hat{\sigma}_3^z) \\ \text{tr}(\rho(14\tau)\hat{\sigma}_3^z) \\ \text{tr}(\rho(15\tau)\hat{\sigma}_3^z) \end{bmatrix}, \tag{D3}$$

respectively. The latter uses time-multiplexing with a constant interval τ, giving a total duration of 15τ.

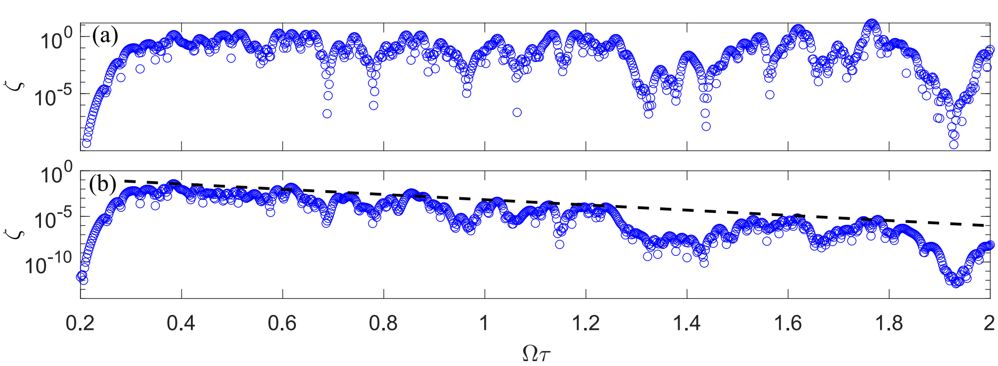

FIG. 5. Determinant of the map as a figure of merit for two-qubit tomography. (a) ζ for the case of Fig. 6(a1). (b) ζ for the case of Fig. 6(b1).

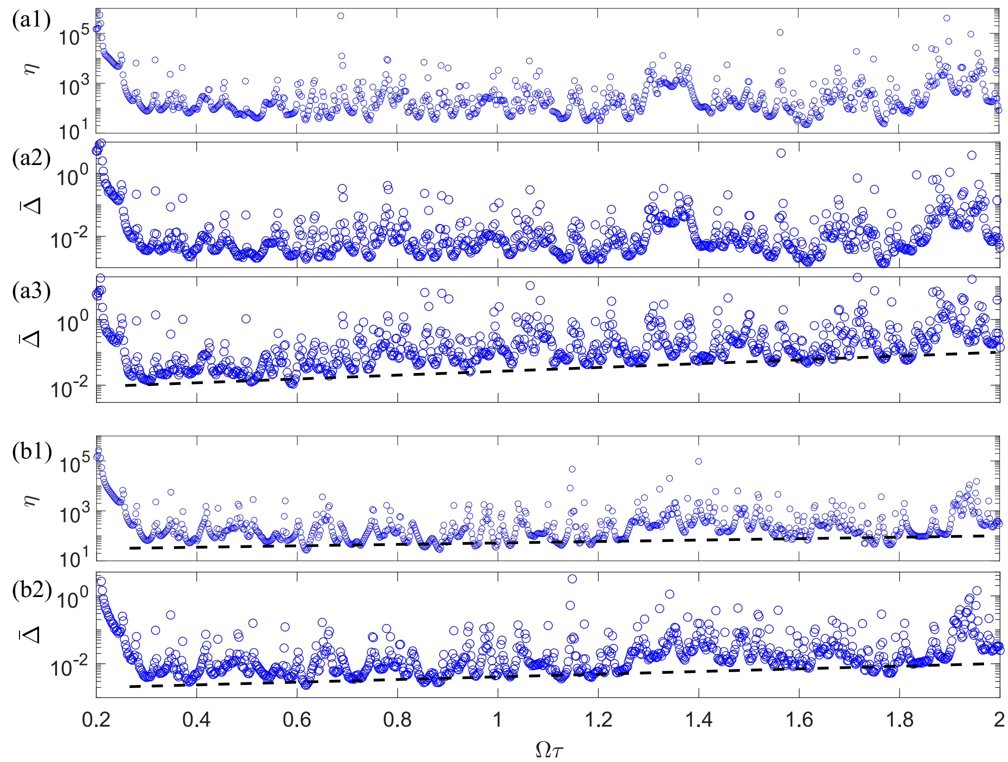

FIG. 6. Exemplary two-qubit tomography with a single-qubit QRN. (a1) The figure of merit $\eta = ||\mathcal{M}||\,||\mathcal{M}^{+}||$ for dynamics without decay. (a2) The corresponding tomographic errors, where we take into account measurement errors with $\xi = 10^{-3}$. (a3) Tomographic errors with the addition of fluctuations of dynamical parameters. (b1) The figure of merit, where the QRN qubit experiences loss of information from energy decay. (b2) The corresponding tomographic errors with energy decay. Dashed lines indicate overall trend.

We present our results for an exemplary realization of the dynamical parameters in Figs. 6(a1) and 6(b2). First, we calculate the figure of merit for the case in which there is no energy decay ($\gamma_3 = 0$) in panel (a1). For a performance test, we plotted the tomographic errors in panel (a2), where each point is an average over 100 random input states. Here, the measurement errors are taken into account with $\xi = 10^{-3}$. Next, we added fluctuations $\nu \in [-1, 1] \times 10^{-2} \times \Omega$ to the system parameters, and we plotted the corresponding tomographic errors in panel (a3). One can see the expected increasing overall trend (dashed line) that is explained in the main text. Since the time-multiplexing is performed 15 times, η computed in panel (a1) still provides a good figure of merit for $15|\nu|\tau \ll 1$. Finally, we incorporate the energy decay of the QRN qubit; see panel (b1) for the figure of merit and (b2) for the corresponding tomographic errors. The increasing overall trend of the errors is directly predicted by the increasing trend of the figure of merit; see the dashed lines in both panels.

[1] J. Biamonte, P. Wittek, N. Pancotti, P. Rebentrost, N. Wiebe, and S. Lloyd, Nature (London) **549**, 195 (2017).

[2] N. Kouda, N. Matsui, H. Nishimura, and F. Peper, Neural Comput. Appl. **14**, 114 (2005).

[3] K. H. Wan, O. Dahlsten, H. Kristjánsson, R. Gardner, and M. Kim, npj Quantum Inf. **3**, 36 (2017).

[4] K. Fujii and K. Nakajima, Phys. Rev. Appl. **8**, 024030 (2017).

[5] S. Ghosh, A. Opala, M. Matuszewski, T. Paterek, and T. C. H. Liew, npj Quantum Inf. **5**, 35 (2019).

[6] K. Beer, D. Bondarenko, T. Farrelly, T. J. Osborne, R. Salzmann, D. Scheiermann, and R. Wolf, Nat. Commun. **11**, 808 (2020).

[7] G. Montavon, G. Orr, and K.-R. Müller, *Neural Networks: Tricks of the Trade* (Springer, 2012), Vol. 7700.

[8] G. Tanaka, T. Yamane, J. B. Héroux, R. Nakane, N. Kanazawa, S. Takeda, H. Numata, D. Nakano, and A. Hirose, Neural Netw. **115**, 100 (2019).

[9] A. Kutvonen, K. Fujii, and T. Sagawa, Sci. Rep. **10**, 14687 (2020).

[10] P. Mujal, Condens. Matter **7**, 17 (2022).

[11] S. Ghosh, A. Opala, M. Matuszewski, T. Paterek, and T. C. H. Liew, IEEE Trans. Neural Netw. Learning Syst. **32**, 3148 (2020).

[12] T. Krisnanda, T. Paterek, M. Paternostro, and T. C. Liew, arXiv:2209.14565 (2022).

[13] T. Krisnanda, K. Dini, H. Xu, W. Verstraelen, and T. C. H. Liew, Phys. Rev. Appl. **19**, 034010 (2023).

[14] Q. H. Tran and K. Nakajima, Phys. Rev. Lett. **127**, 260401 (2021).

[15] S. Ghosh, T. Paterek, and T. C. H. Liew, Phys. Rev. Lett. **123**, 260404 (2019).

[16] T. Krisnanda, S. Ghosh, T. Paterek, and T. C. H. Liew, Neural Netw. **136**, 141 (2021).

[17] S. Ghosh, T. Krisnanda, T. Paterek, and T. C. H. Liew, Commun. Phys. **4**, 105 (2021).

[18] T. Krisnanda, S. Ghosh, T. Paterek, W. Laskowski, and T. C. H. Liew, Phys. Rev. Appl. **18**, 034011 (2022).

[19] S. Ghosh, K. Nakajima, T. Krisnanda, K. Fujii, and T. C. H. Liew, Adv. Quantum Technol. **4**, 2100053 (2021).

[20] P. Mujal, J. Nokkala, R. Martínez-Peña, G. L. Giorgi, M. C. Soriano, and R. Zambrini, J. Phys.: Complexity **2**, 045008 (2021).

[21] H. Xu, T. Krisnanda, R. Bao, and T. C. H. Liew, New J. Phys. **25**, 023028 (2023).

[22] L. C. G. Govia, G. J. Ribeill, G. E. Rowlands, H. K. Krovi, and T. A. Ohki, Phys. Rev. Res. **3**, 013077 (2021).

[23] W. D. Kalfus, G. J. Ribeill, G. E. Rowlands, H. K. Krovi, T. A. Ohki, and L. C. G. Govia, Phys. Rev. Res. **4**, 033007 (2022).

[24] H. Xu, T. Krisnanda, W. Verstraelen, T. C. H. Liew, and S. Ghosh, Phys. Rev. B **103**, 195302 (2021).

[25] R. Martínez-Peña, G. L. Giorgi, J. Nokkala, M. C. Soriano, and R. Zambrini, Phys. Rev. Lett. **127**, 100502 (2021).

[26] W. Xia, J. Zou, X. Qiu, and X. Li, Front. Phys. **17**, 33506 (2022).

[27] M. Negoro, K. Mitarai, K. Fujii, K. Nakajima, and M. Kitagawa, arXiv:1806.10910 (2018).

[28] R. A. Bravo, K. Najafi, X. Gao, and S. F. Yelin, arXiv:2111.10956 (2021).

[29] J. Chen and H. I. Nurdin, Quant. Inf. Proc. **18**, 198 (2019).

[30] J. Chen, H. I. Nurdin, and N. Yamamoto, Phys. Rev. Appl. **14**, 024065 (2020).

[31] J. Nokkala, R. Martínez-Peña, G. L. Giorgi, V. Parigi, M. C. Soriano, and R. Zambrini, Commun. Phys. **4**, 53 (2021).

[32] Z. Denis, I. Favero, and C. Ciuti, Phys. Rev. Appl. **17**, 034077 (2022).

[33] R. A. Horn and C. R. Johnson, *Matrix Analysis* (Cambridge University Press, 2012).

[34] A. Ben-Israel, SIAM J. Numer. Anal. **3**, 585 (1966).

[35] H. Labuhn, D. Barredo, S. Ravets, S. De Léséleuc, T. Macrì, T. Lahaye, and A. Browaeys, Nature (London) **534**, 667 (2016).

[36] P. Scholl *et al.*, Nature (London) **595**, 233 (2021).

[37] I. Carusotto, D. Gerace, H. E. Tureci, S. De Liberato, C. Ciuti, and A. İmamoğlu, Phys. Rev. Lett. **103**, 033601 (2009).

[38] T. Esslinger, Annu. Rev. Condens. Matter Phys. **1**, 129 (2010).

[39] F. Arute *et al.*, Nature (London) **574**, 505 (2019).

[40] J. Herrmann *et al.*, Nat. Commun. **13**, 4144 (2022).

[41] Y. Y. Gao, B. J. Lester, Y. Zhang, C. Wang, S. Rosenblum, L. Frunzio, L. Jiang, S. M. Girvin, and R. J. Schoelkopf, Phys. Rev. X **8**, 021073 (2018).